

Urban Outdoor Measurement Study of Phased Antenna Array Impact on Millimeter-Wave Link Opportunities and Beam Misalignment

Lars Kuger, Aleksandar Ichkov, Petri Mähönen and Ljiljana Simić

Abstract—Exploiting multi-antenna technologies for robust beamsteering to overcome the effects of blockage and beam misalignment is the key to providing seamless multi-Gbps connectivity in 5G-and-beyond mm-wave networks. In this paper, we present the first large-scale outdoor mm-wave measurement study using a phased antenna array in a typical European town. We systematically collect fine-grained 3D angle-of-arrival and angle-of-departure data, totaling over 50,000 received signal strength measurements. We study the impact of phased antenna arrays in terms of number of link opportunities, achievable data rate and robustness under small-scale mobility, and compare this against reference horn antenna measurements. Our results show a limited number of 2–4 link opportunities per receiver location, indicating that the mm-wave multipath richness in a European town is surprisingly similar to that of dense urban metropolises. The results for the phased antenna array reveal that significant losses in estimated data rate occur for beam misalignments in the order of the half-power beamwidth, with significant and irregular variations for larger misalignments. By contrast, the loss for the horn antenna is monotonically increasing with the misalignment. Our results strongly suggest that the effect of non-ideal phased antenna arrays must be explicitly considered in the design of agile beamsteering algorithms.

Index Terms—Millimeter wave, phased antenna array, beam misalignment, multipath propagation, urban deployments.

I. INTRODUCTION

Multi-antenna technologies are the key enabler for unlocking the potential of millimeter-wave (mm-wave) spectrum bands in 5G-and-beyond networks [1], [2]. A number of mm-wave outdoor measurement campaigns, predominantly using channel sounder setups with horn antennas, e.g. [3]–[9], have now demonstrated the fundamental feasibility of mm-wave links in urban environments and resulted in mm-wave statistical channel models (see [10] and references therein). This year has also seen the first test commercial mm-wave outdoor deployments, albeit with limited capabilities and performance [11]. Directional high-gain antenna beams are used to overcome the high path loss at mm-wave frequencies, but the sensitivity to misalignment of antenna beams [6], [12] and the effect of link blockage due to environmental and mobile obstacles such as buildings [13] and humans [14], remain primary challenges for seamless coverage in large-scale mobile network deployments. The key to making mm-wave

cellular networks a reality is thus exploiting multi-antenna technology for robust and precise beamsteering to overcome effects of blockage and beam misalignment caused by large and small-scale mobility, and provide seamless gigabit-per-second (Gbps) connectivity.

Great advances have been reported in the literature regarding mm-wave antenna technology [15]–[17], but the evaluation of these devices has been largely conducted in controlled indoor environments. The notable exceptions to this are [18]–[21], which demonstrated outdoor coverage measurements using mm-wave phased antenna arrays. However, these works lack fine-grained angle-of-arrival (AoA) and angle-of-departure (AoD) measurements, which are crucial for understanding the impact of beam misalignment on mm-wave link and network performance. Other prior outdoor measurement studies, e.g. [3]–[9], used horn antenna or omni-directional antenna setups. The existing literature thus offers very limited insight on the performance of mm-wave antenna arrays in a real outdoor urban network environment, in particular with respect to the beamsteering opportunities and beam misalignment effects, which is an essential input for system-level engineering design of future mm-wave networks.

In this paper, we present the first large-scale outdoor urban mm-wave measurement study using a state-of-the-art phased antenna array, collecting received signal strength (RSS) data over systematic fine-grained 3D AoA and AoD orientations in a typical European town. We study the impact of phased antenna arrays in terms of the number of link opportunities, achievable data rate and robustness under small-scale mobility, and directly compare this against reference measurements using a horn antenna. Our results show a limited number of 2–4 available distinct spatial link opportunities per receiver location, indicating that the mm-wave multipath richness in a typical European town center is surprisingly similar to that in dense urban areas as presented in [3]–[5], [7], [9]. The results for the phased antenna array reveal that losses in estimated data rate of up to 70% occur for small beam misalignments in the order of the half-power beamwidth (HPBW), with significant and irregular variations in estimated data rate for larger beam misalignments due to the non-ideal phased antenna array radiation pattern. By contrast, the loss in estimated data rate for the horn antenna setup is monotonically increasing with the orientation error. This shows that earlier measurement studies [6], [12] or theoretical studies [22], [23] of beam misalignment effects on mm-wave link and network performance using horn antennas or idealized directional antenna patterns cannot be

All authors are with the Institute for Networked Systems, RWTH Aachen University, Kackertstrasse 9, 52072 Aachen, Germany.
E-mail: {lku, aic, pma, lsi}@inets.rwth-aachen.de.

simply generalized. Consequently, we analyze the implications that our results have on the design for future beamsteering algorithms in mm-wave outdoor network deployments.

The rest of the paper is organized as follows. Sec. II gives the related work overview. Sec. III presents our measurement setup and methodology. Our measurement results are presented and analyzed in Sec. IV. In Sec. V we discuss the engineering implication of our findings for outdoor mm-wave network deployments. Finally, Sec. VI concludes the paper.

II. RELATED WORK

Recent years have seen great advances in mm-wave phased antenna arrays and corresponding transceivers for base stations (BSs) and user equipment (UE). For instance, Samsung [17] has presented a 28 GHz base station with a 64-element phased antenna array, IBM and Ericsson [15] have demonstrated a dual-polarized 28 GHz phased antenna array module with 128 elements, and Sivers IMA has released 16-element mm-wave phased antenna array [16]. However, these new mm-wave transceivers and phased antenna array designs have largely been evaluated in controlled environments [15]–[17], rather than in real outdoor urban settings. Notable exceptions to this are the studies in [18]–[21]. In [18], [19], and [20] data rate measurements with 28 GHz multi antenna arrays were conducted in outdoor environments, analyzing the possible coverage in potential mm-wave cells. Yet, these studies did not include detailed AoA or AoD measurements, which are central to understanding the impact of non-ideal, mm-wave phased antenna arrays on the design of beamsteering algorithms for mm-wave networks. In [21] the RSS over AoD was measured at several receiver positions in a car park using an omnidirectional antenna at the receiver and a 60 GHz phased antenna array at the transmitter side, finding strong reflected paths for many receiver positions. However, [21] did not investigate beamsteering opportunities and limitations caused by beam misalignment, due to the lack of AoA data. By contrast, in this work we present the results of the first comprehensive large-scale urban measurement campaign with mm-wave phased antenna arrays systematically collecting RSS over fine-grained AoA and AoD antenna orientations.

Independently from the advances in mm-wave multi-antenna technology, a number of mm-wave measurement campaigns have been conducted in outdoor environments with the aim of establishing statistical mm-wave channel models (see [2] and references therein). Rappaport *et al.* [3] conducted seminal measurements at 28, 38, 60 and 70 GHz in Austin, Texas, and New York City using a sliding correlator channel sounder with mechanically steerable horn antennas to record the power delay profile for a limited selected range of AoA and AoD combinations at each TX/RX pair. Similar measurement methodologies have been employed in other measurement campaigns, e.g. [4], [5], [7]–[9], and measurement-based statistical channel models such as the NYU model [25] have consequently been proposed (see [10] and references therein). Overall, analyzing the number of potential link opportunities, the studies in [3]–[5], [7], [9] reported a limited number of 2–5 mm-wave multipath clusters per TX/RX pair for urban

areas in different metropolises. However, as these measurements campaigns were conducted with horn or omnidirectional antenna setups, they do not allow us to study the impact of phased antenna arrays on potential link opportunities and beam misalignment in mm-wave networks. By contrast, in this work we collected RSS data with mm-wave phased antenna arrays over fine-grained AoA and AoD sample points to study these open questions. Additionally, we conducted measurements in a typical European town rather than a big city like prior studies in the literature.

Lee *et al.* [12] studied the effect of beam misalignment based on measurements taken with a channel sounder and horn antennas. To that end, power measurements were systematically collected across azimuth angles at 28 and 38 GHz in both free-space and urban environments. The general conclusion based on these horn antenna measurements was that for a fixed beamwidth, the power loss increases linearly with increasing beam misalignment until saturation is reached. This confirms the results of Simić *et al.* in [6], where the RSS over AoA and AoD was systematically measured with a horn antenna setup in an urban environment in the 60 GHz band. The results in [6], [12] stand in stark contrast to the results of our phased antenna array measurements in this paper, which show a non-linear relationship between misalignment and power loss. To demonstrate that this is caused by the non-ideal, phased antenna array pattern, we also explicitly compare our measurements against those with a horn antenna in the same outdoor scenarios. Our comparison underlines the paradigm shift that occurs in terms of beam misalignment effects when moving from horn antennas to real phased antenna arrays.

In addition to empirical research, the effect of beam misalignment on mm-wave network performance has also been addressed from a theoretical perspective, e.g. in [22], [23]. These approaches typically make use of simple and idealized antenna radiation pattern models to investigate the effect of fundamental antenna parameters such as beamwidth on various metrics of system performance. Moreover, analyses regarding beam misalignments have mainly focused on misalignments smaller than the main lobe beamwidth [22]. Wildman *et al.* [23] do consider larger beam misalignments from a theoretical perspective and show that in theory sidelobes can be beneficial to the success probability of a transmission in low density networks and that the spatial throughput and transmission capacity maximizing beamwidth has a nearly linear relationship with the mean orientation error for Gaussian and sectored antenna radiation pattern models. As such idealized radiation pattern models are much more similar to a horn antenna radiation pattern than that of a real mm-wave phased antenna array, our results strongly suggest that such a linear relationship will not hold in real mm-wave deployments and that the severe consequences of this idealization on the requirements and opportunities of beamsteering algorithms and network system design have been underestimated. Therefore, our work forms a basis for realistic models of beam misalignment effects in urban 5G-and-beyond mm-wave networks.

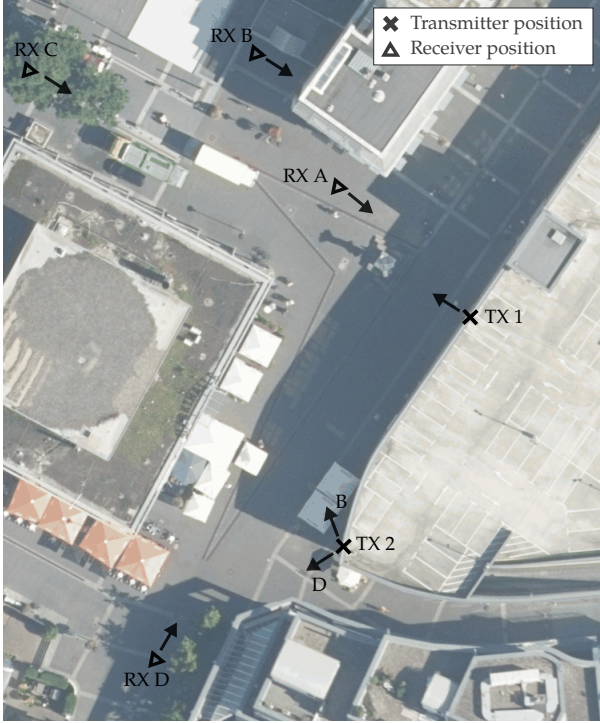


Fig. 1: Aerial view of the TX (1-2) and RX positions (A-D), with the initial antenna orientations indicated by an arrow. The measurement scenarios are listed in Table I. (Photo courtesy of [26]).

III. MEASUREMENT SETUP & METHODOLOGY

Our outdoor measurement campaign was conducted in the German town of Langenfeld. The measurement area constitutes the central pedestrian zone with mainly shops in the surroundings and only delivery trucks being allowed to enter. The buildings typically have 2-5 floors and are constructed of concrete with large windows and some metal parts on the facades. The measurements were conducted over the course of 12 days during the summer of 2018, with dry weather and temperatures of around 25° C.

The transmitter (TX) was located at different positions on the rooftop of a multi-floor car park at a height of 9.7 m. The receiver (RX) positions A–D were located in the pedestrian zone, i.e. on ground level, with the mounted antenna at a height of 1.7 m. Fig. 1 shows an aerial image of the area where the TX positions (1, 2) and RX positions (A, B, C, D) are marked. Fig. 2 shows the different TX and RX positions during the measurements. The RX is circled in green and the TX in orange. In case the LOS is blocked, a green square indicates the geometric LOS direction. The positions were chosen based on representative scenarios as follows:

- *TX1-RXA*: Typical scenario for small cell, with clear LOS and TX-RX distance of 25 m (Figs. 2a-2b).
- *TX1-RXB and TX2-RXB*: RX-B was chosen to investigate the effects of an obstructed LOS and evaluate the coverage from different TX positions for the same RX position. In scenario TX1-RXB the LOS is partially blocked by a building corner, while in scenario TX2-RXB the LOS

is partially blocked by a lamp-post with a flower box mounted on it (Figs. 2c-2f).

- *TX1-RXC*: Represents a typical street canyon with 18 m width and buildings to the left and to the right. The large TX-RX distance of 65 m makes this representative of cell-edge distances in a mm-wave small cell. The LOS path was predominantly clear despite tree foliage (Figs. 2g-2h).
- *TX2-RXD*: Scenario chosen to investigate the effect of tree foliage on mm-wave coverage, with a TX-RX distance of 28 m and clearly visible trees obstructing the LOS (Figs. 2i - 2j).

For our measurement campaign we used two different 60 GHz transceiver setups, one utilizing a phased antenna array and the other utilizing a standard horn antenna for comparison. A relatively narrowband signal transmission was chosen (1 MHz) to obtain fine-grained RSS and angle orientation data, allowing us to have a robust setup that does not require strict calibration as the gain over the frequency band is flat and the time-component of the channel is not recorded. Importantly, since we are not interested in a time-characterization of the channel, the narrowband power measurements are sufficient for our objective of characterizing mm-wave link opportunities in a typical outdoor environment and beamsteering requirements for maintaining a reliable link connectivity under small-scale mobility. Both setups utilize software-defined radios (SDRs), facilitating transport and use in different locations. We note that the frequency bands in the range of 24–86 GHz are under consideration for 5G-and-beyond mm-wave cellular networks [27]. In this paper, we report measurements in the 60 GHz band without the loss of generality, due to equipment availability and for comparability with prior mm-wave outdoor urban measurement studies, e.g. [3], [6], [18], [21].

A. Phased Antenna Array Setup

We used the SiversIMA 60 GHz phased antenna array radio frequency integrated circuit (RFIC) TRX BF/01 [24] with the corresponding evaluation kit EVK06002 [28]. The setup is capable of operating in the frequency range from 57 GHz–71 GHz. The included RF module uses direct conversion in both TX and RX mode. It includes a 16+16 (TX/RX) patch antenna module, with each antenna array consisting of 16×2 microstrip patch antenna elements directly connected to the RFIC [16]. Fig. 3a shows a schematic drawing of the phased antenna array board and the RFIC. The phase weights and amplitudes are applied to the signal in the analog RF domain using 16 independent RF paths. Thus, only azimuth plane beamsteering is allowed in the range [+45°, −45°], based on a codebook with up to 64 different antenna pattern entries. The phased array transceiver was controlled via a USB interface.

Figs. 3c-3d compare the measured phased antenna array radiation pattern with the simulated one obtained using MATLAB's phased antenna array toolbox based on generic patch antenna elements. We note the considerable differences between the ideal simulated radiation pattern and the real, non-ideal measured radiation pattern.

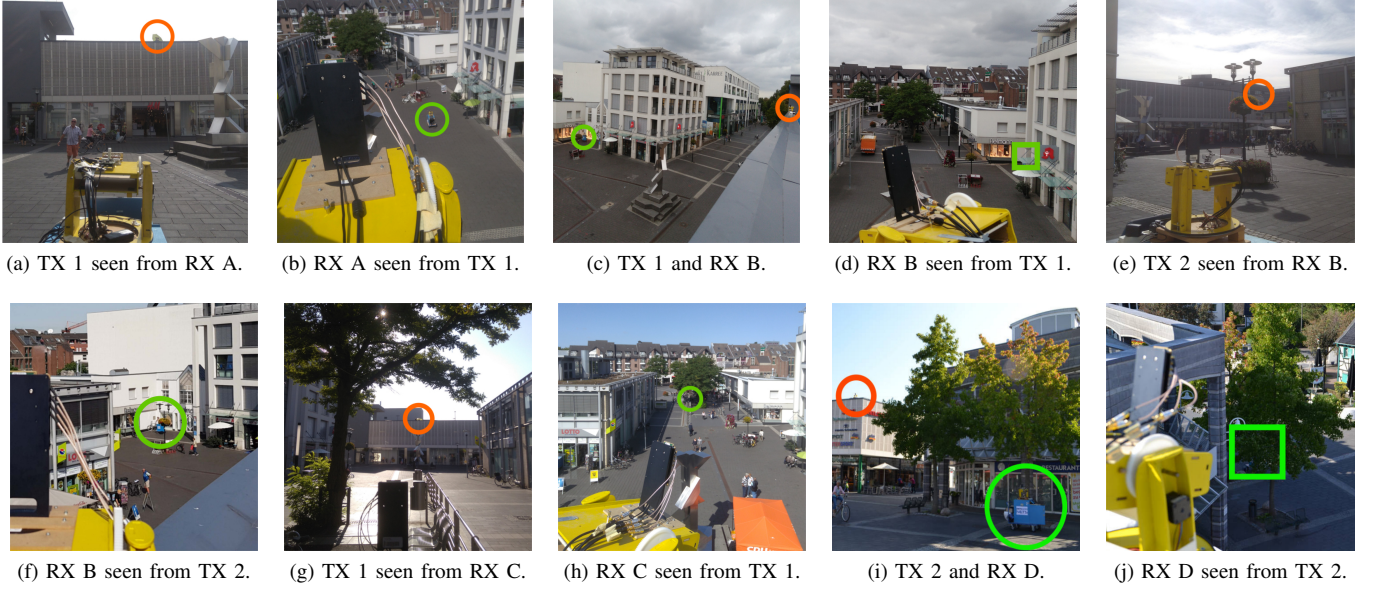


Fig. 2: TX and RX in different positions during measurements. The RX is circled in green and TX in orange. In case the LOS is blocked, a green square indicates the geometric LOS direction.

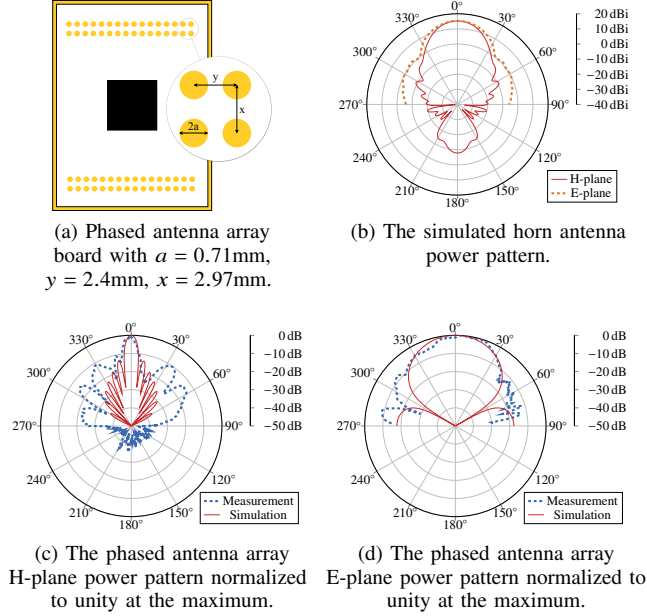


Fig. 3: Schematic drawing of the SiversIMA TRX BF/01 phased antenna array board and antenna radiation patterns.

The schematic of the overall phased antenna array setup is shown in Fig. 4. The left part of the figure shows the TX including host PC 1, USRP X310 SDR with LFTX daughterboards, and the phased antenna array transceiver. The right part of the figure shows the RX consisting of an equivalent setup. The host PC 1 generates a complex sinusoidal signal at the frequency $f_{sin} = 250$ kHz and streams it to the USRP. The USRP generates a baseband signal with a sampling

rate $f_s = 1$ MHz which is fed to the phased antenna array transceiver. The phased antenna array transceiver upconverts the signal to a frequency $f_c = 58.32$ GHz, and transmits the signal over the air. The RX phased antenna array downconverts the received signal and feeds it to the USRP, which samples the signal with a sampling rate $f_s = 1$ MHz. The complex samples are streamed to the host PC 2, where the power spectrum of the received signal is computed using a flattop window. Finally, the signal strength $RSS_{A,meas}$ of the received sinusoidal signal is extracted from the power spectrum, which was calibrated against an Agilent E4440A spectrum analyzer.

B. Horn Antenna Setup

For comparison, our second setup used the FC1005V/00 V-band converter by SiversIMA [29] and a standard 15 dBi gain horn antenna by Flann Microwave [30]. The FC1005V/00 is capable of up- and downconverting to and from 57-66 GHz using an intermediate frequency (IF) bandwidth of 1-5 GHz. Fig. 3b shows the simulated radiation pattern of the standard gain horn antenna.

The schematic of the horn antenna setup is shown in Fig. 5. The left part of the figure shows the TX including the host PC 1, USRP N210 with WBX daughterboard, Sivers IMA FC1005V/00 upconverter and the horn antenna. The right part of the figure shows the RX consisting of a similar setup as the TX. The transmission and reception signal chain of the horn antenna setup is equivalent to the phased antenna array setup (cf. Sec. III-A), except that the signal between the USRP and up-/downconverter is at the intermediate frequency $f_{IF} = 1.32$ GHz and not at baseband. The RSS at the horn antenna setup $RSS_{H,meas}$ was obtained by the same calibrated procedure as described in Sec. III-A.

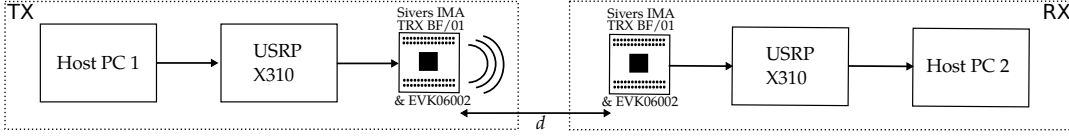


Fig. 4: Schematic of the phased antenna array setup. Link distance d depends on the TX/RX locations.

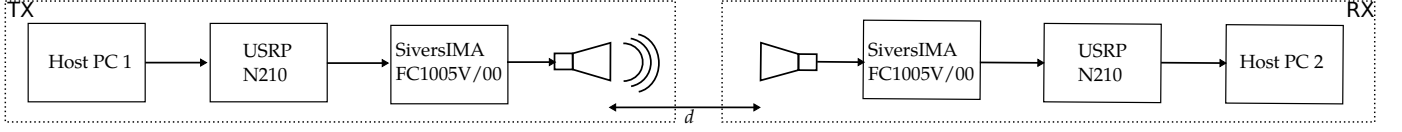
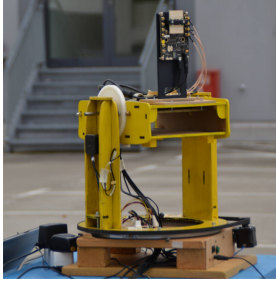
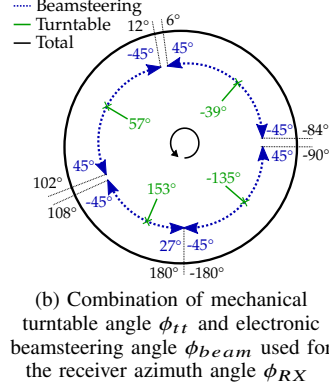


Fig. 5: Schematic of the horn antenna setup. Link distance d depends on the TX/RX locations.



(a) 3D turntable with mounted antenna array transceiver



(b) Combination of mechanical turntable angle ϕ_{tt} and electronic beamsteering angle ϕ_{beam} used for the receiver azimuth angle ϕ_{RX}

Fig. 6: Automated 3D turntable with mounted antenna array transceiver used in the measurements.

C. Measurement Procedure

To identify potential link opportunities and their respective antenna orientations (AoD, AoA), we systematically swept the angular space by changing the beam orientations at the TX and RX. Each beam orientation can be characterized by a pair of azimuth and elevation angles (ϕ , θ). As the phased antenna array transceiver only allows beamsteering in a 90° azimuth range and the horn antenna setup cannot electronically steer its beam, we have used a custom made 3D turntable to help cover the complete angular space with additional mechanical movements when the range of electronic beamsteering was exceeded. The turntable uses two stepper motors for azimuth and elevation movement. The automated 3D turntable with the mounted phased antenna array transceiver is shown in Fig. 6a.

1) *Phased Antenna Array Transceiver*: For the measurements, we covered all orientations within azimuth $\phi_{RX} \in [-180^\circ, 180^\circ]$ and elevation $\theta_{RX} \in [-30^\circ, 60^\circ]$ at each RX position. The range of elevation angles was chosen based on observation of potential link opportunities, taking into account the positioning of the TX and RX. The elevation resolution of $\Delta\theta_{RX} = 30^\circ$ was chosen based on the E-plane HPBW of 36° found in the phased antenna array radiation pattern measurements (cf. Fig. 3d). The azimuth resolution was chosen to be $\Delta\phi = 6^\circ$ corresponding to the HPBW of the azimuth-plane radiation pattern (cf. Fig. 3c). To change the azimuth angle orientation at the RX, we used a combination of

mechanical movement by the 3D turntable and the electronic beamsteering, $\phi_{RX} = \phi_{tt} + \phi_{beam}$, as shown in Fig. 6b. The measurement time per RX orientation (ϕ_{RX}, θ_{RX}) was 1 second. A complete sweep over all RX orientations for a single fixed TX orientation took 500 s.

Once such an RX sweep was finished, the TX changed its azimuth orientation and another RX measurement run was started. Analogously to the RX, the transmitting phased antenna array transceiver was mounted on a 3D turntable, with the elevation angle fixed to $\theta_{TX} = -15^\circ$ based on the large E-Plane HPBW and the higher positioning on the rooftop of a parking lot. The azimuth angle of the TX orientation was changed in $\Delta\phi_{TX} = 6^\circ$ steps by a combination of mechanical turntable movement and electronic beamsteering, as described previously. The range of azimuth angles to be covered was chosen to be $\phi_{TX} \in [-90^\circ, 84^\circ]$ w.r.t. the initial TX antenna orientation. Hence, the total measurement time for all TX/RX combinations with the phased antenna array setup was 30×500 s, or 4 hours and 10 minutes. The overall angular coverage per position is presented in Table I.

2) *Horn Antenna Array Transceiver*: To mechanically steer the transceiver in various orientations, the horn antenna RX setup was mounted on a 3D turntable, similar to that shown in Fig. 6a for the phased antenna array. For the measurements, we chose to cover all RX azimuth angles $\phi_{RX} \in [-180^\circ, 180^\circ]$ with a resolution $\Delta\phi_{RX} = 6^\circ$, identical to the phased antenna array setup, so that the obtained results can be readily compared. Furthermore, we chose to cover the range of elevation angles $\theta_{RX} \in [-30^\circ, 60^\circ]$ with a higher resolution than for the phased antenna array setup, i.e. $\Delta\theta_{RX} = 10^\circ$, to allow a finer-grained identification of AoA and identify potential scattering or reflecting objects. On the transmitter side, the horn antenna setup was also mounted on a 3D turntable and the elevation angle was fixed to $\theta_{TX} = -15^\circ$, as used for the phased antenna array and in accordance with the broad E-Plane HPBW of 34° (cf. Fig. 3b).

A measurement run for a fixed transmitter orientation took considerably longer using the horn antenna setup than using the phased antenna array setup, due to the fact that all movements in elevation or azimuth were achieved by mechanical movement of the 3D turntable. To strike a balance between the time spent for measurements with each setup, we limited the range of horn antenna TX azimuth angles per measurement position, ensuring that a minimum range of 54° centered

TABLE I: Measurements scenarios with ID consisting of a number (TX position), capital letter (RX position) and small letter (setup: (a) phased antenna array and (h) horn antenna). The distance d is the 3D link distance. $N_{meas,tot}$ is the total number of measured TX/RX beam orientation combinations.

ID	TX	RX	d (m)	Type	Setup	$\theta_{TX}(^\circ)$	$\phi_{TX}(^\circ)$	$\theta_{RX}(^\circ)$	$\phi_{RX}(^\circ)$	$N_{meas,tot}$
1Aa	1	A	25.3	LOS	Array	-15	-90:6:84	-30:30:60	-180:6:174	7200
1Ah	1	A	25.3	LOS	Horn	-15	-54:6:42	0:10:60	-180:6:174	7140
1Ba	1	B	43.8	NLOS	Array	-15	-90:6:84	-30:30:60	-180:6:174	7200
1Bh	1	B	43.8	NLOS	Horn	-15	-54:6:6	0:10:60	-180:6:174	4620
1Ca	1	C	64.9	LOS	Array	-15	-90:6:84	-30:30:60	-180:6:174	7200
1Ch	1	C	64.9	LOS	Horn	-15	-24:6:30	-30:10:60	-180:6:174	6000
2Da	2	D	27.8	NLOS	Array	-15	-72:6:52	-30:30:60	-180:6:174	5200
2Ba	2	B	63.2	NLOS	Array	-15	-90:6:84	-30:30:60	-180:6:174	7200

TABLE II: System parameters of the antenna setups and the wideband 5G NR system model.

	Horn ant. setup	Phased ant. array setup	Wideband 5G-NR model
Main lobe gain G (dBi)	15	16	–
EIRP (dBm)	9.61	3.95	25
Sensitivity S (dBm)	-91	-104	-74.4

around the LOS direction was systematically covered with a $\Delta\phi_{TX} = 6^\circ$ granularity. The overall angular coverage per position is presented in Table I.

D. Post-Processing of Measurement Data

In our analysis in Sec. IV, we take two different perspectives on our measurement results. First, we study the link opportunities in a typical European town in Sec. IV-A, i.e. we are essentially interested in the path loss that a signal experiences between TX and RX for different antenna orientations. Therefore, we present the RSS of both measurement setups for a normalized nominal link budget so as to eliminate effects that may occur due to different antenna gains or different equivalent isotropically radiated powers (EIRPs) between the measurement setups. Second, we estimate the achievable data rate in mm-wave cells to analyze the effect of beam misalignment on the link performance, presented in Sec. IV-B. To this end, we assume the TX to be a BS operating at a fixed EIRP, and estimate the achievable data rates at the receiving UE based on our measurements. In the following, we detail the post-processing steps taken to obtain the data presented in Sec. IV-A and Sec. IV-B from our RSS measurements.

RSS with Normalized Nominal Link Budget: We obtain the normalized RSS for the phased antenna array setup RSS_A and the horn antenna setup RSS_H from the measured RSS $RSS_{A,meas}$ and $RSS_{H,meas}$, respectively, by making equal the nominal link budget for both measurement setups, i.e.

$$RSS_A = RSS_{A,meas} + C_c, \quad (1)$$

$$RSS_H = RSS_{H,meas}. \quad (2)$$

The constant C_c is the difference between the actual link budgets of the measurement setups, i.e.

$$C_c = EIRP_H + G_H - (EIRP_A + G_A), \quad (3)$$

where $EIRP_H$ and $EIRP_A$ are the EIRPs of the horn antenna setup and the phased antenna array setup during the measurements, respectively, and G_H and G_A are the estimated main lobe antenna gains of the horn antenna and the phased antenna array, respectively. The values of these parameters are given in Table II. We note that the validity of our results is not compromised by this operation as the sensitivity of the phased antenna array setup $S_{A,meas}$ was considerably lower than the sensitivity of the horn antenna setup $S_{H,meas}$. The sensitivity of our overall measurement system after the normalization is still limited by the horn antenna measurement setup, i.e.

$$S = \max\{S_{H,meas}, S_{A,meas} + C_c\} = -91 \text{ dBm}. \quad (4)$$

The normalized received signal strengths RSS_A and RSS_H obtained after this post-processing operation are presented in Sec. IV-A.

Estimating Achievable Data Rate: To analyze the effect of beam misalignment on the link performance in mm-wave cells, we mapped $RSS_{A,meas}$ and $RSS_{H,meas}$ to the estimated achievable data rate T , assuming a fixed BS EIRP of $EIRP_{BS} = 25$ dBm, in line with existing regulations for wideband transmissions at 60 GHz [31]. First, the measured received signal strengths $RSS_{A,meas}$ and $RSS_{H,meas}$ were scaled according to the additional power that receivers would receive for a BS transmitting with $EIRP_{BS}$, i.e.

$$RSS'_A = RSS_{A,meas} + (EIRP_{BS} - EIRP_A), \quad (5)$$

$$RSS'_H = RSS_{H,meas} + (EIRP_{BS} - EIRP_H). \quad (6)$$

The overall sensitivity S' of our overall measurement system is then given by

$$S' = \max\{S_{H,meas} + (EIRP_{BS} - EIRP_H), S_{A,meas} + (EIRP_{BS} - EIRP_A)\} \quad (7)$$

$$= -75.61 \text{ dBm}. \quad (8)$$

To then map RSS'_A and RSS'_H to the estimated, achievable data rate T for a wideband system, we used the Verizon 5G-NR model which demonstrated a maximum throughput of 4 Gbps using an 800 MHz bandwidth [32]. An attenuated and

truncated version of the Shannon bound is used as a mapping function, similar to those used for modeling of link adaption in LTE [33] and for 5G NR coexistence in [34], i.e.

$$T = \begin{cases} 0 & \text{for } SNR < SNR_{min}, \\ \alpha W \log_2(1 + SNR) & \text{for } SNR_{min} \leq SNR \text{ and } SNR \leq SNR_{max}, \\ T_{max} & \text{for } SNR > SNR_{max}, \end{cases} \quad (9)$$

where $W = 800$ MHz denotes the system bandwidth, $\alpha = 0.75$ is the correction factor to account for implementation losses, $SNR_{min} = -4.5$ dB, and $SNR_{max} = 20$ dB¹. The modeled receiver is assumed to have a noise figure of $NF = 10$ dB and implementation loss of $L_I = 5$ dB such that the SNR is calculated from our data as

$$SNR = RSS'_{A/H} - (N + NF + L_I) \quad (10)$$

where $N = 10 \log_{10}(kBT)$ with Boltzmann constant k is the thermal noise for assumed temperature $T = 290$ K. The estimated data rate ranges from $T_{min} = 263$ Mbps for $SNR_{min} = -4.5$ dB to $T_{max} = 4$ Gbps for $SNR_{max} = 20$ dB. We note that this post-processing step does not compromise the validity of our measured data since the sensitivity S' is still sufficiently low to ensure detection of all signals that result in a data rate greater than zero, i.e.

$$SNR(RSS = S') = -5.61 \text{ dB} < SNR_{min}. \quad (11)$$

The estimated data rate T obtained after this post-processing operation is presented in Sec. IV-B.

IV. MEASUREMENT RESULTS & ANALYSIS

In this section, we present the results of the measurement campaign outlined in Sec. III. In Sec. IV-A, we analyze available link opportunities in terms of the observed multipath clusters based on measured RSS, and we trace the corresponding independent physical propagation paths between TX and RX. In Sec. IV-B, we analyze the effects of beam misalignment on the estimated achievable mm-wave data rate.

A. Link Opportunities & AoA Analysis

In the following, we study significant link opportunities that were found during our measurement campaign, trace the corresponding physical propagation paths on an environment map and analyze the observed differences between the phased antenna array and horn antenna measurement data. To that end, we present our results as follows. Figs. 7-8 present the RSS versus RX orientations in a heatmap which allows us to investigate the structure of received multipath clusters. Here we assume for each RX orientation (ϕ_{RX}, θ_{RX}) the best corresponding transmitter orientation ϕ_{TX} found during the measurements, in order to show the full set of multipath clusters available at each receiver location. Fig. 9 illustrates the same underlying data as in Figs. 7-8 in terms of the AoA

¹We point out that, even though we give SNR_{min} and SNR_{max} in dB-scale for better comprehensibility, the formula to convert to data rate in (9) requires SNR in linear units

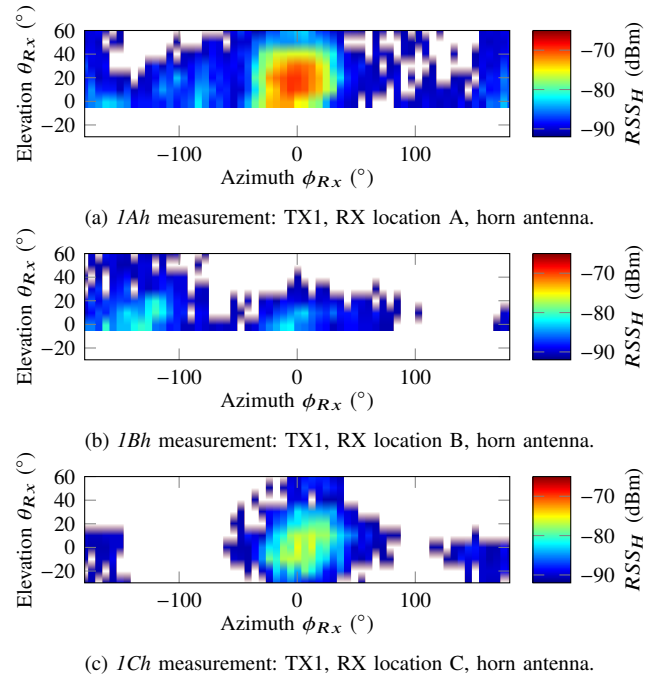


Fig. 7: RSS versus RX orientation for *horn antenna* measurements at different TX-RX locations (assuming optimal TX orientation).

and how it is related to the environment, showing polar plots of the RSS in a schematic environment map of the study area. Finally, we present Fig. 10 where we trace the corresponding independent physical propagation paths between TX and RX based on the AoA, AoD, and potential reflectors in the study area. In the following, our results are presented based on Figs. 7-10 location-by-location.

We start our analysis with a typical scenario for a mm-wave small cell with a clear LOS, i.e. at RX location A. As expected, a strong LOS cluster is observed for both the horn antenna and the phased antenna array measurement setup in the heatmaps in Fig. 7a and Fig. 8a, respectively. Nonetheless, we observe the distinct effect of the different antenna patterns on the RSS measured with respect to the RX steering angle. While the horn antenna measurement in Fig. 7a exhibits a smooth cluster, the same cluster appears irregular for the phased antenna array measurement shown in Fig. 8a². Similarly, the AoA polar plot for scenario 1A in Fig. 9a allows us to clearly recognize the impact of the horn antenna and phased antenna array radiation patterns (*cf.* Fig. 3b–3c). The consequence of this is that the non-ideal, phased antenna array radiation pattern makes it much more difficult to identify true independent propagation paths. For instance, let us consider in Fig. 9a the AoA polar plot, which exhibits several peaks for the phased antenna array RSS. The first peak around $\phi_{RX} = 0^\circ$ points in the LOS direction. Additionally, we observe peaks around $\phi_{RX} = -30^\circ$,

²In Fig. 8, we note that the measurement points are not spaced equidistantly over azimuth angles ϕ_{RX} . This is due to the imperfect beam steering with the manufacturer-supplied beambook, i.e. we observed an offset between the beam steering angle that we set and the actual angle of the main lobe seen at the over-the-air interface. We measured the offset for all beamsteering angles and correct for these offsets during the post-processing of the results.

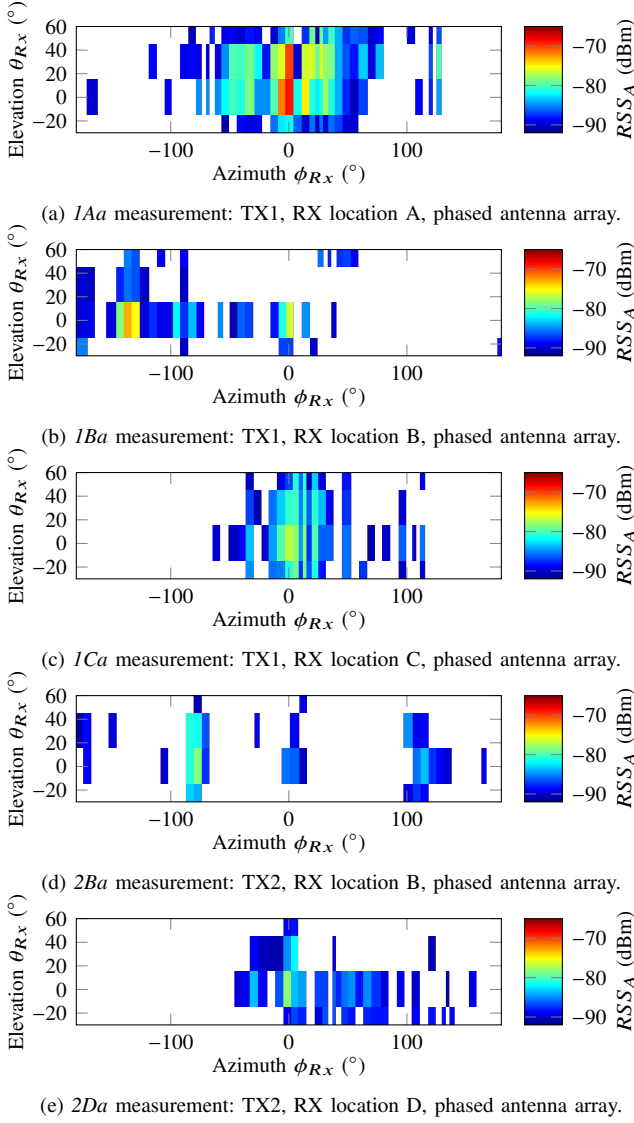


Fig. 8: RSS versus RX orientation for *phased antenna array* measurements at different TX-RX locations (assuming optimal TX orientation).

$\phi_{RX} = 30^\circ$, $\phi_{RX} = -84^\circ$, and $\phi_{RX} = 127^\circ$. Taking into account AoD information (not shown for brevity), we can identify that the high RSSs at $\phi_{RX} = -84^\circ$ and $\phi_{RX} = 127^\circ$ correspond to independent secondary NLOS paths, which are shown in the environment map in Fig. 10a. By contrast, the high RSSs around $\phi_{RX} = -30^\circ$ and $\phi_{RX} = 30^\circ$ are due to sidelobes that point into the LOS direction, thereby falsely indicating independent propagation paths. This is clear when looking at the map in Fig. 9a, as there are no reflectors at $\phi_{RX} = -30^\circ$ and $\phi_{RX} = 30^\circ$ from the RX. However, this may cause problems to beamsteering algorithms that do not have information about the environment and the AoD. For instance, an algorithm may generate a list of orientations supposedly corresponding to viable independent propagation paths during initial beam training. Then in the case of detected blockage on the primary path, it may switch to a falsely indicated propagation path, i.e. it switches to a sidelobe over

the same path. Consequently, it would fail to overcome the link blockage.

We next consider RX location B. Again we start our analysis by comparing the heatmap of the horn antenna measurement in Fig. 7b with the heatmap of the phased antenna array measurement in Fig. 8b. In line with the observations for RX location A, we note the significant differences between the cluster appearance for horn antenna and phased antenna array measurements. However, in contrast to the results at RX location A, two almost equally strong multipath clusters are observed for RX location B. Fig. 9b shows the AoA polar plot for the measurement scenario *IB*. Combining knowledge of the AoA, the environment, and the steered phased antenna array radiation pattern, we can trace the two physical propagation paths as shown in Fig. 10a, where the NLOS path likely included the reflection from a shop window. Nonetheless, we observe again that tracing the physical propagation paths is difficult purely based on AoA information (*cf.* Fig. 9b), as previously described for receiver location A. In contrast to the measurement *IAa*, we point out that AoD information is not helpful in measurement scenario *IBa* to distinguish between a true independent propagation path and a sidelobe-induced high RSS. The reason is that the AoD is the same for both the LOS and NLOS path (*cf.* Fig. 10a) with our AoD measurement resolution of around 6° . Overall, we can draw two conclusions based on these observations. On the one hand, the observation of having multiple link opportunities is promising for mm-wave system designers as it suggests that mm-wave coverage can also be provided for urban scenarios with a partly blocked LOS. On the other hand, our results suggest that even knowing both AoA and AoD may not be sufficient to reliably identify true independent propagation paths. Instead, we used both *a priori* environment information and knowledge of the real steered phased antenna array radiation pattern to identify such independent propagation paths. In practice, future commercial mobile mm-wave systems will not have such perfect, *a priori* information. Consequently, other strategies will be needed to identify true independent propagation paths. For instance, in scenarios with high link budget, using a nearly omni-directional radiation pattern at the receiver to record the power delay profile may allow extracting the number of independent propagation paths based on time of arrival [7]. Alternatively, environment-awareness will be essential for robust mm-wave beamsteering.

Let us now consider RX location C to investigate a LOS scenario that is similar to that of RX location A. The differences are an increased TX-RX distance and the fact that RX C is positioned in an 18 m wide street canyon with buildings to either side. Nonetheless, the heatmap of the horn antenna measurement in Fig. 7c and the phased antenna array measurement in Fig. 8c strongly resemble the heatmaps obtained for RX location A (*cf.* Fig. 7a and Fig. 8a, respectively). We combine the knowledge of the AoA shown in Fig. 9c, AoD (not shown here for brevity) and the knowledge of the environment to trace the independent NLOS paths for RX location C. These are shown in the environment map in Fig. 10a. However, we emphasize that these are difficult to trace solely based on the AoA polar plot in Fig. 9c due to the

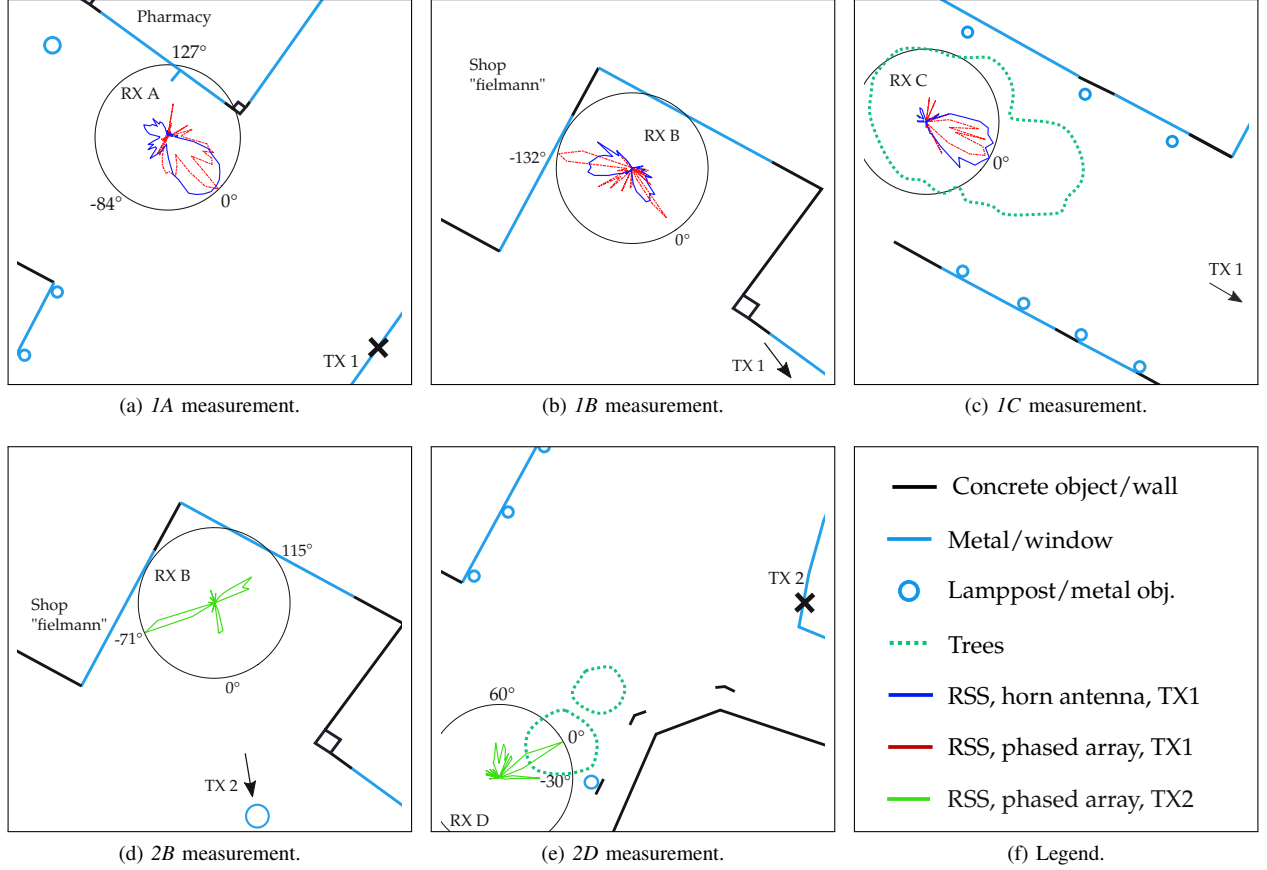


Fig. 9: Illustrated RSS over azimuth angles per TX-RX pair. The RSS polar plots are normalized to the maximum RSS per RX location to focus on the AoA analysis.

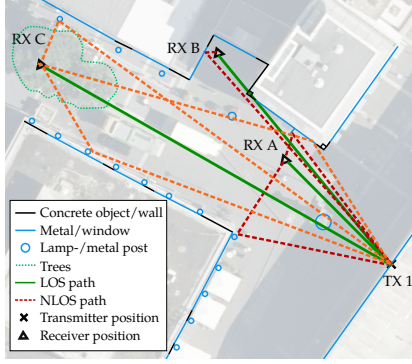
irregular, phased antenna array radiation pattern. For instance, the AoA at RX location C (cf. Fig. 9c) looks similar to the AoA at RX location A (cf. Fig. 9a). Yet, at RX location A the high RSS at angle $\phi_{RX} = 30^\circ$ is caused by a sidelobe whereas it corresponds to a true independent propagation path at RX location C. This underlines the difficulty of identifying viable independent physical propagation paths by one-sided RSS measurements.

Let us now investigate measurements that were conducted with the TX at location TX 2, i.e. at the corner of the car park. First, we consider the RX location B for which we already discussed the measurement results from a transmitter at location TX 1. Again the LOS is obstructed, this time by a lamppost with a flower box mounted on it. The distance between TX 2 and RX B was 63 m. Fig. 8d shows the heatmap for the TX 2 - RX B pair, where we note several multipath clusters, the strongest received around $\phi_{RX} = -71^\circ$. Fig. 9d shows the corresponding AoA polar plot, where we can see the peaks around $\phi_{RX} = -71^\circ$, $\phi_{RX} = 115^\circ$, and $\phi_{RX} = 0^\circ$. All three orientations correspond to true independent signal propagation paths as shown in the environment map in Fig. 10b. The signal was likely reflected at several shop windows. The independent propagation paths were traced and distinguished from sidelobe-induced high RSS using information about the environment and the steered RX

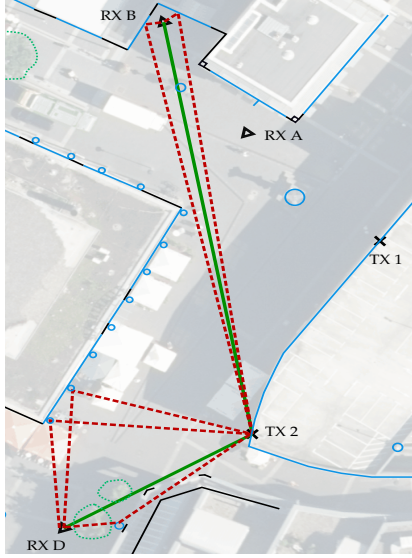
phased antenna array radiation pattern (not shown here for brevity). The latter does not have sidelobes that could have caused a high RSS at these RX orientations. We emphasize that AoD information cannot help to distinguish true independent propagation paths from sidelobes, as previously described for measurement 1Ba. Overall, these results support the previous observations that multiple mm-wave link opportunities can be found even in distant and NLOS scenarios in the given urban environment, but identifying independent propagation paths requires combined knowledge from different sources, i.e. environmental awareness, beyond pure RSS measurements.

Finally, we evaluate the measurement results from RX location D where the LOS path from the transmitter in location TX 2 was obstructed by the foliage of a tree. Nevertheless, the heatmap in Fig. 8e shows higher RSS values at $\phi_{RX} = 0^\circ$, i.e. in the direction of the transmitter, than for other orientations. The path loss for the LOS path is 8 dB higher than free space path loss, likely due to the foliage. In addition to the LOS path, we can identify NLOS paths based on the AoA polar plot in Fig. 9e, AoD (not shown here for brevity), and knowledge of the environment. Metal columns in front of a building and a lamppost likely reflected the signals as shown in the environment map in Fig. 10b.

Overall, our measurements show 2–4 multipath clusters per receiver position. Reflections were mainly caused by metal or



(a) Signal paths from transmitter 1.



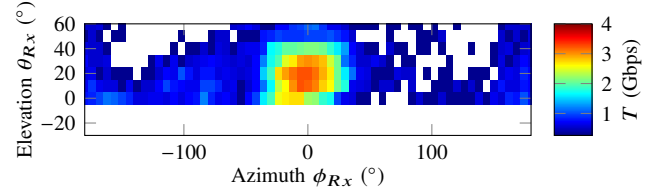
(b) Signal paths from transmitter 2.

Fig. 10: Maps showing the LOS/NLOS path traces from the different TX and RX positions. The materials of buildings and other objects are also indicated.

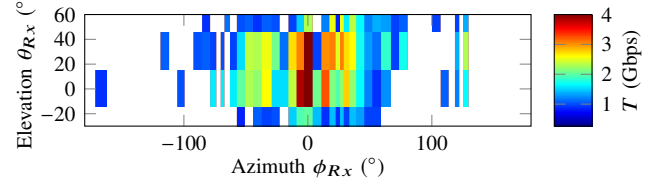
glass on facades and, somewhat surprisingly, by lampposts, enabling potential NLOS links in multiple scenarios. We observed significant differences between the measurements with the phased antenna arrays as compared to measurements with the horn antenna. In particular, we noted that determining independent propagation paths purely based on one-sided phased antenna array RSS measurements was not a reliable approach. Instead, knowledge of both AoA and AoD, and of the actual environment, was needed to identify such independent propagation paths. Additionally, due to small-scale movements of a user or non-ideal beam training, the transmitter and the receiver may not be perfectly aligned. In Sec. IV-B we therefore present an analysis of the effects of beam misalignment at transmitter and receiver on achievable data rates of the mm-wave link opportunities revealed by our measurements.

B. Analysis of Beam Misalignment Effects

In this section we study the effect of beam misalignment on the link performance in outdoor mm-wave networks, using



(a) Scenario 1Ah: TX1, RX location A, horn antenna.



(b) Scenario 1Aa: TX1, RX location A, phased antenna array.

Fig. 11: Estimated data rate versus RX orientation for scenario 1A (assuming optimal TX orientation).

the estimated achievable data rate as calculated from (9) as the performance metric. We emphasize that considering the achievable data rate rather than solely RSS measurements (as in Sec. IV-A) allows us to better understand and assess the networking consequences of misaligned beams, especially with regard to higher system layers that need to cope with the resulting changes in the achievable PHY data rate. To illustrate this, in Fig. 11 we show the heatmap of estimated data rate versus RX orientation for RX location A (cf. Fig. 7a and Fig. 8a for the corresponding RSS versus RX orientation heatmaps). From the heatmap in Fig. 11b, it is evident that a phased antenna array beam misalignment of a few degrees in the azimuth can result in a dramatic loss in data rate.

In real mm-wave outdoor deployments such beam misalignments can occur for several reasons. Fig. 12 illustrates several typical scenarios, where we consider the BS to be the transmitter and the UE to be the receiver, i.e. the downlink. After successful initial beam training, the BS and UE are ideally perfectly aligned. However, imperfect beam training due to e.g. stale beam training data or ambiguous information about independent propagation paths (as described in Sec. IV-A) may result in beam misalignments. Such beam misalignments can occur at the BS and at the UE as shown in Fig. 12a. Additionally, a UE beam misalignment may be caused by a rotation of the device, as illustrated in Fig. 12b. Fig. 12c shows how a small-scale lateral movement of the UE out of the BS's beam causes a beam misalignment at both BS and UE. The UE may then readjust its beam orientation to try and mitigate the effects of the BS beam misalignment, as illustrated in Fig. 12d. In the following, we analyze how these beam misalignment scenarios affect the estimated achievable data rate based on our measured RSS data. We note that even though we focus our analysis on the downlink scenario, the general causes for beam misalignment as shown in Fig. 12 are the same for the uplink case.

1) *BS Beam Misalignment Analysis:* After initial beam training, mobile users in a mm-wave network can cause a BS beam misalignment for example by physically moving out of the BS's beam (cf. Fig. 12c). Similarly, imperfect beam train-

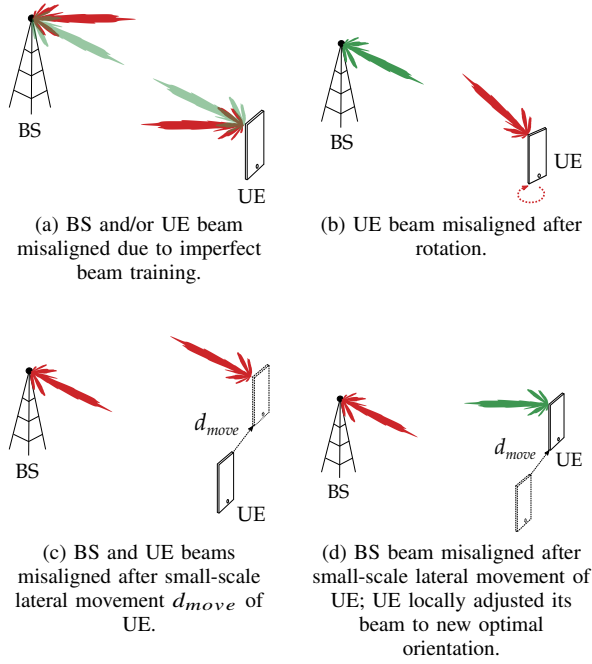


Fig. 12: Scenarios illustrating potential beam misalignments at BS and UE.

ing may result in a BS beam misalignment (*cf.* Fig. 12a). In this section, we study the residual loss in estimated achievable data rate for such BS beam misalignments, assuming that the UE locally adjusts its orientation dynamically to mitigate the BS beam misalignment effects (*cf.* Figs. 12a and 12d). Namely, we consider

$$T(\Delta_{TX}) = \max_{\phi_{RX}, \theta_{RX}} T(\Delta_{TX}, \phi_{RX}, \theta_{RX}), \quad (12)$$

where Δ_{TX} is the beam misalignment with respect to the best possible BS orientation $\phi_{TX, best}$, i.e.

$$\Delta_{TX} = \phi_{TX} - \phi_{TX, best}, \quad (13)$$

$$\phi_{TX, best} = \arg \max T(\phi_{TX}, \phi_{RX}, \theta_{RX}). \quad (14)$$

We neglect the elevation misalignment based on the assumption that all UEs are in the same plane, such that the BS's elevation beam misalignment is negligible as compared to the BS's elevation HPBW of 36° . We note that the best possible BS orientation corresponds to LOS links for the scenarios 1A, 1C, and 2D, and to NLOS links for the scenarios 1B and 2B.

In Fig. 13 we show the estimated achievable data rate T of a link over the BS (TX) beam misalignment Δ_{TX} with respect to the best possible BS orientation $\phi_{TX, best}$. Based on Figs. 13a–13b we make three observations about beam misalignment for our phased antenna array setup. First, we observe that the maximum data rate is only achieved without beam misalignment, i.e. there is only one maximum peak. Second, small beam misalignments in the order of the HPBW cause significant losses in data rate of up to 70%. For instance, a beam misalignment of -7° in scenario 1A produces a drop from 4 Gbps to 1.4 Gbps and from 2.6 Gbps to 0.8 Gbps in scenario 2D. Third, the loss in data rate is not increasing monotonically with increasing beam misalignment. Overall,

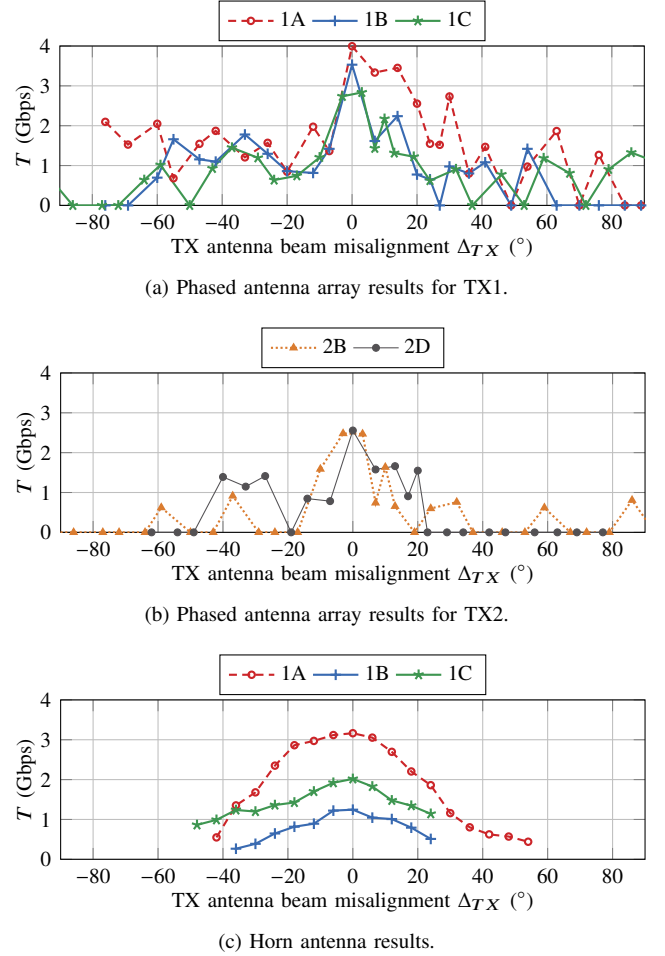


Fig. 13: The estimated data rate T versus the BS (TX) beam misalignment Δ_{TX} with respect to the best possible link (assuming optimal ϕ_{RX} , θ_{RX}).

the results in Figs. 13a–13b demonstrate that a UE locally adjusting its orientation is not sufficient to fully mitigate the effects of BS beam misalignment. Consequently, strategies for tracking UE movement at the BS are required to maintain high data rates. Moreover, given the observed non-monotonic relationship between beam misalignment and loss in data rate, we expect that some types of beam tracking algorithms will not work reliably. For instance, let us consider an RSS-gradient-following beam tracking approach, i.e. an algorithm that tries to find the ideal beam orientation by adapting the beam orientation of its phased antenna array beam to a neighboring orientation that achieves a higher RSS. Due to the observed irregular variation of the achievable data rate over increasing beam misalignment, it would not be able to find the global optimal orientation.

In Fig. 13c, we present the estimated maximum data rate over the horn antenna BS beam misalignment for comparison with the phased antenna array results. We observe that the data rates decrease monotonically with increasing misalignment which is in contrast to the observations made in Figs. 13a–13b for the phased antenna array. We emphasize that this stark dissimilarity between the results for the antenna types indicates

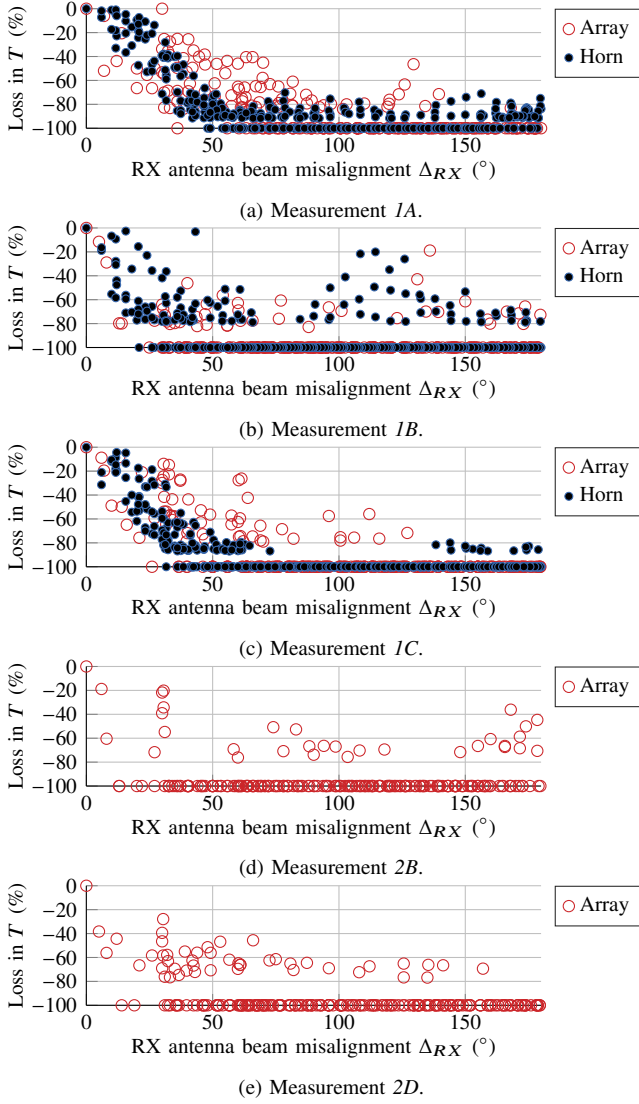


Fig. 14: Loss in estimated data rate T versus UE (RX) beam misalignment Δ_{RX} with respect to the best possible link (assuming optimal ϕ_{TX}).

that we cannot simply infer the impact of beam misalignments on mm-wave links based on measurements taken with horn antennas as in e.g. [6], [12] or calculations based on simplistic directional antenna radiation pattern models as in e.g. [23]. Instead, realistic phased antenna array radiation patterns have to be explicitly taken into account in the design of beam training and tracking algorithms.

2) *UE Beam Misalignment Analysis:* In Figs. 12b–12c we illustrated how a rotation or small-scale movement of the UE may result in a UE beam misalignment. Similarly, imperfect beam training as shown in Fig. 12a may lead to a UE beam misalignment. In this section, we study the effects of such UE beam misalignments, assuming that the BS locally adjusts its orientation dynamically to mitigate the UE beam misalignment effects. We thus apply the same principle of considering one-sided misalignment only, as in the previous analysis of the BS

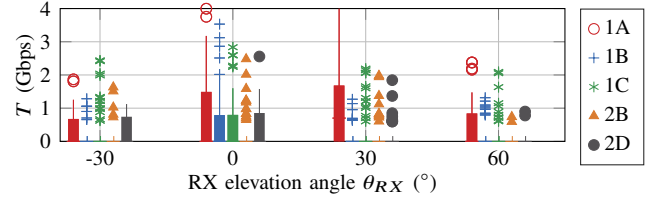


Fig. 15: Boxplots of the estimated data rate T that can be achieved with the phased antenna array over all UE azimuth angles ϕ_{RX} with a fixed UE elevation angle θ_{RX} (assuming optimal ϕ_{TX}).

beam misalignment. Namely, we consider

$$T(\Delta_{RX}) = \max_{\phi_{TX}} T(\phi_{TX}, \Delta_{RX}). \quad (15)$$

where Δ_{RX} is the beam misalignment with respect to the best possible UE orientation $(\phi_{RX,best}, \theta_{RX,best})$ comprising both the azimuth and elevation misalignment, i.e.

$$\Delta_{RX} = \sqrt{(\phi_{RX} - \phi_{RX,best})^2 + (\theta_{RX} - \theta_{RX,best})^2}, \quad (16)$$

$$(\phi_{RX,best}, \theta_{RX,best}) = \arg \max T(\phi_{TX}, \phi_{RX}, \theta_{RX}). \quad (17)$$

In Fig. 14 we present the loss in estimated data rate T for a UE (RX) antenna beam misalignment Δ_{RX} with respect to the best possible UE orientation. Figs. 14a–14c show results for both measurement setups, where we again observe that a misalignment causes a gradual loss in data rate for the horn antenna results, whereas the phased antenna array results vary rather irregularly. This confirms that we cannot simply infer the impact of beam misalignments on mm-wave links based on measurements taken with horn antennas. Moreover, in Figs. 14a–14e we find that a small misalignment of the UE phased antenna array beam of up to 8° results in losses of data rate between 6–60%. This demonstrates that even with perfect UE tracking, agile beamsteering at the UE is needed to compensate residual losses in data rate due to misalignment.

One key to enabling mm-wave networks is to successfully integrate UE phased antenna arrays that can reliably maintain a connection over all 3D orientations. As described in Sec. III-A, the phased antenna array used in our measurements only allows azimuth beamsteering while having a wide elevation HPBW of 36° . To investigate if this is a suitable configuration for a mm-wave UE, we isolate the effect of the UE elevation angle on estimated data rates. We expect that the best data rate would be achieved for the measured elevation angles θ_{RX} that are closest to the ideal elevation orientation towards the BS, which can be computed from the distances between BS and UE (cf. Table I). Namely, we expect the scenarios 1A and 2D to achieve approximately equal maximum estimated achievable data rate for $\theta_{RX} = 0^\circ$ and $\theta_{RX} = 30^\circ$, as the distances between BS and UE was the shortest in these cases, implying a greater elevation angle. For larger distances between BS and UE, the ideal elevation angle is smaller and we expect to see the maximum estimated achievable data rate for the scenarios 1B, 1C, and 2B at $\theta_{RX} = 0^\circ$.

Fig. 15 shows boxplots of the estimated data rate T over all azimuth angles $\phi_{RX} \in [-180^\circ, 180^\circ]$ for UE elevation angle θ_{RX} , i.e. we consider

$$T(\theta_{RX}) = \max_{\phi_{TX}} T(\phi_{TX}, \phi_{RX}, \theta_{RX}). \quad (18)$$

We observe a drop in maximum estimated data rate for all results except 1A when the elevation angle is not equal to 0° . This is expected, except for the result 2D which shows an outlier achieving around 2.6 Gbps for $\theta_{RX} = 0^\circ$. This may be due to the tree foliage that blocked the LOS between TX and RX (cf. Fig. 2i). Overall, despite the large HPBW of the phased antenna array pattern in the elevation plane of 36° , the loss in the maximum achievable estimated data rate ranges between 26% and 70% for a change in elevation angle θ_{RX} from 0° to 60° over all results presented in Fig. 15. Therefore, we conclude that 2D beamsteering will not be sufficient to fully exploit available UE link opportunities in a 3D environment.

3) *Two-sided Beam Misalignment Analysis:* In the previous sections, we treated the effects of BS and UE beam misalignment separately. However, in real outdoor mm-wave network deployments, a misalignment at both BS and UE is likely to occur simultaneously (cf. Fig. 12). We now study this case for the phased antenna array results, i.e. the beamsteering opportunities at the UE for a given BS beam misalignment. To this end, in Figs. 16-17 we show the estimated data rate T over UE (RX) azimuth angles ϕ_{RX} for selected measurement scenarios and for selected representative BS (TX) orientations ϕ_{TX} . In Figs. 16-17 we only consider the UE elevation angle $\theta_{RX} = 0^\circ$, which was observed to achieve the highest data rates over all elevation angles (cf. Fig. 15).

In Fig. 16 the BS orientations ϕ_{TX} were selected to study the effects of *small-scale* misalignment in the order of the HPBW of around 6° . From Fig. 16 it is evident that the UE achieves the highest estimated data rate and has the maximum number of viable orientations when the transmitter is well aligned, i.e. $\phi_{TX} = 0^\circ$ or $\phi_{TX} = \pm 3^\circ$. A small-scale misalignment of the transmitter of $\pm 7^\circ$ to $\pm 10^\circ$ produces a significant decrease in the maximum estimated data rate of up to 54%. For a misalignment in the order of $\pm 7^\circ$ at both BS and UE, the loss in estimated data rate is 38%–100% with a median of 70% across all our results. Overall, we conclude that the joint effect of small-scale beam misalignment at BS and UE results in severe losses in data rate, placing the burden on agile beamtracking algorithms to update BS and UE orientation at a sufficient rate to ensure robustness of high data rate links for mobile users.

In Fig. 17 the BS orientations ϕ_{TX} were selected to study link opportunities that occur due to sidelobes or independent secondary propagation paths, i.e. at orientations that deviate at *large-scale* from the best orientation. In Fig. 17a, for $\phi_{TX} = 30^\circ$ the overall estimated data rates are below those for $\phi_{TX} = 0^\circ$, but the shape of the curve is similar. This suggests that the transmitter has a sidelobe towards the receiver when oriented at $\phi_{TX} = 30^\circ$, using the same propagation path as for $\phi_{TX} = 0^\circ$. By contrast, we observe an independent secondary (NLOS) propagation path for $\phi_{RX} = -84^\circ$ and $\phi_{TX} = 41^\circ$ which was also traced on the environment map

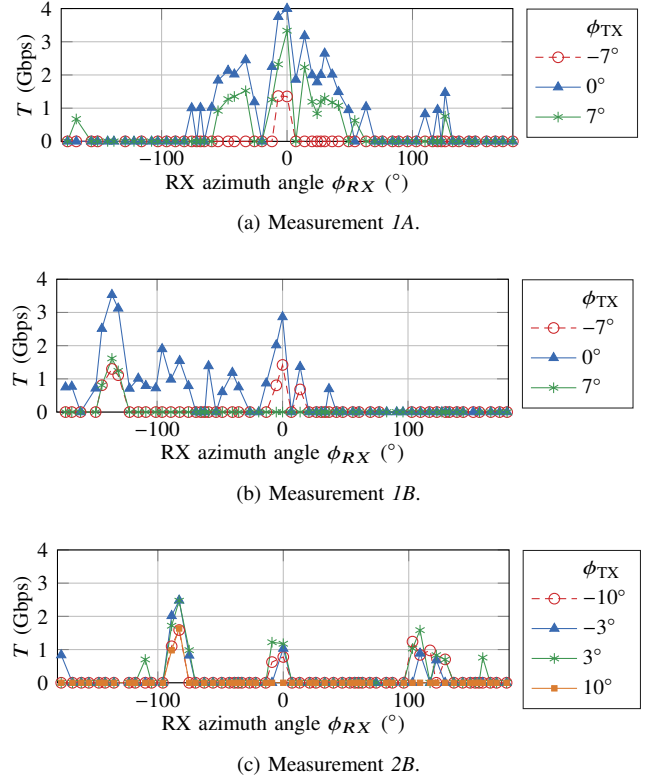


Fig. 16: Estimated data rate T versus RX azimuth angles ϕ_{RX} for selected measurements and selected fixed BS orientations ϕ_{TX} , representative of small-scale BS beam misalignment ($\theta_{RX} = 0^\circ$ assumed throughout).

of the study area (cf. Fig. 10a). Fig. 17b reveals the same trend. The ϕ_{RX} -dependent link opportunities for $\phi_{TX} = -37^\circ$ are similar to those for $\phi_{TX} = 3^\circ$, suggesting that they resulted from a sidelobe of the transmitter. For $\phi_{TX} = -29^\circ$, a distinct signal path with a receiver orientation of $\phi_{RX} = 35^\circ$ yields the highest estimated data rate (cf. Fig. 10a for the map of the study area). Finally, in Fig. 17c two independent secondary propagation paths for $\phi_{TX} = -33^\circ$ and $\phi_{TX} = 17^\circ$ are observed. Based on the results in Fig. 17, we conclude that identifying an independent secondary propagation path between BS and UE solely based on measured data rates or signal quality over either AoD or AoA data is very difficult, as sidelobes may also allow good data rates using the primary signal path. An approach of combining information from BS, UE, and external sources such as motion sensors or other environmental awareness, e.g. [35], [36], may therefore be needed to identify independent secondary propagation paths that can be used to overcome blockage which may occur on the primary path.

V. DISCUSSION

Our mm-wave measurements in a German town center showed a limited number of 2–4 multipath clusters per receiver position, which is similar to the results reported for dense urban areas in modern metropolises [3]–[6]. This stands in contrast to expectations that the differences in building types

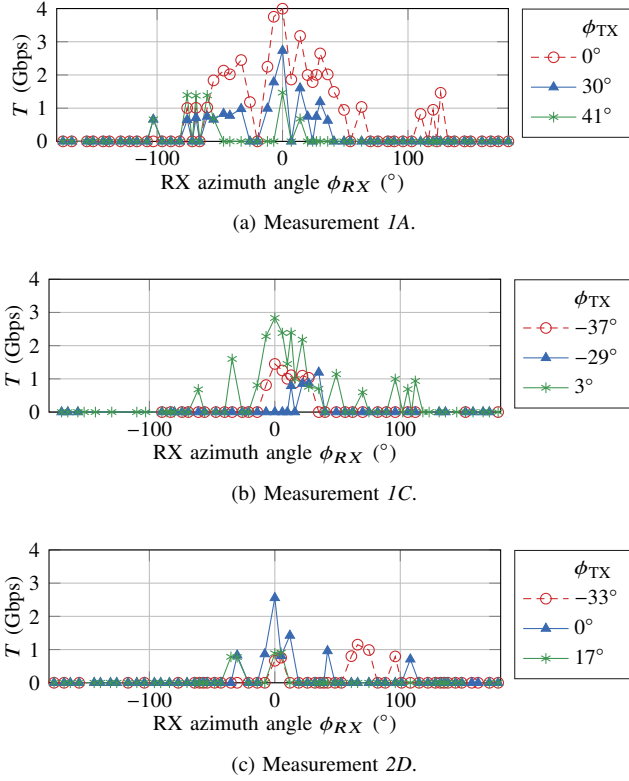


Fig. 17: Estimated data rate T versus RX azimuth angles ϕ_{RX} for selected measurements and selected fixed BS orientations ϕ_{TX} , representative of large-scale BS beam misalignment ($\theta_{RX} = 0^\circ$ assumed throughout).

and layout between a typical European town and dense urban areas in modern metropolises would have an effect on the number of mm-wave multipath clusters. Our results thus suggest that it is possible to cover such small cities with mm-wave Gbps-networks at limited infrastructure cost, as the area of such city centers is rather small and suitable base station sites are, thanks to the building structure, easier to find than in more metropolitan areas. This suggests that mm-wave phased antenna arrays and mm-wave massive MIMO-type deployments are an attractive approach to achieve Gbps data rates in such environments.

However, looking more closely at the structure of the received multipath clusters, we observe the paradigm shift that occurs when moving from horn antennas to real phased antenna arrays. The clusters exhibit a smooth structure when measured with the horn antenna which has a radiation pattern without strong sidelobes or nulls, thereby giving a good indication of the actual underlying physical propagation paths. The same physical propagation paths are perceived very differently with the phased antenna array: the clusters appear irregular. This is a consequence of the real phased antenna array which has a non-ideal radiation pattern with significant sidelobes and nulls, as shown in Figs. 3c–3d. We also note that such strong sidelobes in the radiation pattern may result in significant intra-cell interference, which will have to be carefully considered during mm-wave network system design. Yet, this fact has been given only very little attention in the existing literature.

As observed throughout this paper, the antenna radiation pattern plays a similarly crucial role in the effects of mm-wave beam misalignment. Our measurements with horn antennas show a monotonic relationship between misalignment and loss in received power, as also presented in earlier studies [6], [12]. By contrast, this does not hold for our phased antenna array results. For azimuth beam misalignments larger than the HPBW the degradation of estimated data rate is not monotonic with increasing beam misalignment for the non-ideal, phased antenna array radiation pattern. Instead, it varies irregularly with increasing beam misalignment. Consequently, measurement results obtained with horn antennas cannot simply be generalized to also hold for phased antenna arrays when investigating the effect of beam misalignment on the expected performance of real mm-wave networks. Similar implications hold for the theoretical works that make use of simplistic idealized antenna patterns, e.g. [22], [23].

Our results also showed that a small-scale beam misalignment at one station, i.e. either at BS or UE, caused a significant loss in estimated data rate that cannot be mitigated fully by the other station. We expect such a one-sided misalignment to be particularly harmful in uplink situations. As mm-wave UEs will likely not be able to feature phased antenna arrays of the same size as BSs, their antenna gain will be more limited due to the smaller number of antenna elements. Moreover, due to the limited battery capacity of the UE, also its output power will be more limited than the BS's output power. While the link performance could still be acceptable under beam misalignment when the BS transmits with high EIRP, this may not be the case under beam misalignments in uplink scenarios, where the UE EIRP is likely to be significantly lower. Thus, we expect to see a large asymmetry between uplink and downlink performance in mm-wave networks. Overall, we conclude that both the BS and UE in mm-wave networks will need to frequently adjust their orientation to counteract even one-sided small-scale beam misalignments.

Furthermore, we note that one of the key challenges for enabling mm-wave outdoor networks is the handling of dynamic blockages by using an independent secondary unblocked signal path, as e.g. pedestrian blockage typically only concerns one multipath cluster and other multipath clusters remain unaffected [7]. However, due to the strength of sidelobes in non-ideal, phased antenna array radiation patterns, our results suggest that it may be difficult to distinguish between a true independent secondary propagation path and a link opportunity due to a sidelobe. This distinction is crucial, as link opportunities due to sidelobes on the primary propagation path are also affected by blockage of the primary propagation path. Beamsteering algorithms that obtain a list of viable link opportunities based on a simple RSSI search, e.g. IEEE 802.11ad-like algorithms [37], are thus expected to suffer from this ambiguity if they do not restart at least a partial beam search upon link blockage.

Finally, our analysis suggest that, despite the wide elevation HPBW of our phased antenna array of 36° , 2D beamsteering is not sufficient to fully exploit available link opportunities at certain receiver positions. These results agree with the findings in [38] where it was demonstrated that 3D rotations can result

in strong link degradations. This is particularly relevant as many beamsteering algorithms proposed in the literature only consider the planar case [38]. We expect that 3D beamsteering and hand-grip aware beamcombining [39] will be required to maintain a high data rate under rotation of the user device and different user activities. Despite the already increasing complexity of 5G-and-beyond protocol design, even additional external information, location-based environmental awareness, shared beamsteering information from devices in direct vicinity of a UE, or local data from a motion tracking sensor may further enhance the robustness and seamless coverage of mm-wave deployments under user mobility.

VI. CONCLUSIONS

We presented the results of the first comprehensive large-scale outdoor mm-wave measurement study using a state-of-the-art phased antenna array in a European town. The data obtained over more than 5,000 systematic fine-grained AoA/AoD combinations per TX/RX pair was analyzed with respect to the number of available link opportunities and the effect of beam misalignment at the receiver and transmitter on the estimated mm-wave link data rate, and compared to reference measurements taken with a horn antenna. Our results show a limited number of 2–4 available multipath clusters per receiver location, indicating that the mm-wave multipath richness in a European town is surprisingly similar to that in dense urban metropolises as presented in prior literature. The results for the phased antenna array reveal that losses in the estimated data rate of up to 70% occurred for small beam misalignments in the order of the HPBW, with significant and irregular variations in the estimated data rate for larger beam misalignments, caused by the non-ideal, phased antenna array radiation pattern. This stands in stark contrast to the horn antenna reference measurements, where the loss in estimated data rate was observed to be monotonically increasing with the misalignment error. Moreover, our results suggest that the characteristics of non-ideal, phased antenna array radiation patterns should be explicitly considered during the design and testing of mm-wave beamsteering algorithms. To this end, our ongoing work is focused on conducting further measurements in more diverse urban scenarios, explicitly studying the performance of beamsteering and beamtracking algorithms based on data obtained with real mm-wave phased antenna arrays.

REFERENCES

- [1] T. S. Rappaport, S. Sun, R. Mayzus, H. Zhao, Y. Azar, K. Wang, G. N. Wong, J. K. Schulz, M. Samimi, and F. Gutierrez, "Millimeter wave mobile communications for 5G cellular: It will work!" *IEEE Access*, 2013.
- [2] M. Xiao, S. Mumtaz, Y. Huang, L. Dai, Y. Li, M. Matthaiou, G. K. Karagiannis, E. Björnson, K. Yang, C. I. and A. Ghosh, "Millimeter wave communications for future mobile networks," *IEEE J. Sel. Areas Commun.*, vol. 35, no. 9, pp. 1909–1935, Sep. 2017.
- [3] T. S. Rappaport, G. R. MacCartney, M. K. Samimi, and S. Sun, "Wideband millimeter-wave propagation measurements and channel models for future wireless communication system design," *IEEE Trans. Commun.*, vol. 63, no. 9, pp. 3029–3056, Sep. 2015.
- [4] M. Samimi, K. Wang, Y. Azar, G. N. Wong, R. Mayzus, H. Zhao, J. K. Schulz, S. Sun, F. Gutierrez, and T. S. Rappaport, "28 GHz angle of arrival and angle of departure analysis for outdoor cellular communications using steerable beam antennas in New York City," in *Proc. IEEE VTC*, Jun. 2013.
- [5] S. Hur, Y. J. Cho, T. Kim, J. Park, A. F. Molisch, K. Haneda, and M. Peter, "Wideband spatial channel model in an urban cellular environments at 28 GHz," in *Proc. IEEE EuCAP*, May 2015.
- [6] L. Simić, N. Perpinias, and M. Petrova, "60 GHz outdoor urban measurement study of the feasibility of multi-Gbps mm-wave cellular networks," in *Proc. IEEE INFOCOM Workshops*, Apr. 2016.
- [7] R. J. Weiler, M. Peter, W. Keusgen, and M. Wisotzki, "Measuring the busy urban 60 GHz outdoor access radio channel," in *Proc. IEEE ICUWB*, Sep. 2014.
- [8] S. Rajagopal, S. Abu-Surra, and M. Malmirchegini, "Channel feasibility for outdoor non-line-of-sight mmwave mobile communication," in *Proc. IEEE VTC*, Sep. 2012.
- [9] J. Ko, Y. Cho, S. Hur, T. Kim, J. Park, A. F. Molisch, K. Haneda, M. Peter, D. Park, and D. Cho, "Millimeter-wave channel measurements and analysis for statistical spatial channel model in in-building and urban environments at 28 GHz," *IEEE Transactions on Wireless Communications*, vol. 16, no. 9, pp. 5853–5868, Sep. 2017.
- [10] T. S. Rappaport, Y. Xing, G. R. MacCartney, A. F. Molisch, E. Mellios, and J. Zhang, "Overview of millimeter wave communications for fifth-generation (5G) wireless networks-with a focus on propagation models," *IEEE Trans. Antennas Propag.*, vol. 65, no. 12, pp. 6213–6230, Dec. 2017.
- [11] S. Segan. (2019) Here's the real truth about Verizon's 5G network. PC Mag Digital Group. [Online]. Available: <https://www.pcmag.com/news/367659/heres-the-real-truth-about-verizons-5g-network>
- [12] J. Lee, M.-D. Kim, J.-J. Park, and Y. J. Chong, "Field-measurement-based received power analysis for directional beamforming millimeter-wave systems: Effects of beamwidth and beam misalignment," *ETRI Journal*, vol. 40, no. 1, pp. 26–38, 2018.
- [13] H. Zhao, R. Mayzus, S. Sun, M. Samimi, J. K. Schulz, Y. Azar, K. Wang, G. N. Wong, F. Gutierrez, and T. S. Rappaport, "28 GHz millimeter wave cellular communication measurements for reflection and penetration loss in and around buildings in New York City," in *Proc. IEEE ICC*, June 2013.
- [14] V. Raghavan, L. Akhoondzadeh-Asl, V. Podshivalov, J. Hulten, M. A. Tassoudji, O. H. Koymen, A. Sampath, and J. Li, "Statistical blockage modeling and robustness of beamforming in millimeter-wave systems," *IEEE Trans. Microw. Theory Tech.*, vol. 67, no. 7, pp. 3010–3024, July 2019.
- [15] B. Sadhu, A. Paidimarri, M. Ferriss, M. Yeck, X. Gu, and A. Valdes-Garcia, "A 128-element dual-polarized software-defined phased array radio for mm-wave 5G experimentation," in *Proc. ACM mmNets Workshop*, New Delhi, India, 2018.
- [16] I. Aziz, R. Dahlbäck, E. Öjefors, A. Rydberg, and D. Dancila, "High Gain Compact 57-66 GHz Antenna Array for Backhaul & Access Communications," in *Proc. IEEE EuCAP*, Apr. 2018.
- [17] F. Aryanfar, J. Pi, H. Zhou, T. Henige, G. Xu, S. Abu-Surra, D. Psychoudakis, and F. Khan, "Millimeter-wave base station for mobile broadband communication," in *Proc. IEEE MTT-S IMS*, May 2015.
- [18] V. Raghavan, A. Partyka, A. Sampath, S. Subramanian, O. H. Koymen, K. Ravid, J. Cezanne, K. Mukkavilli, and J. Li, "Millimeter-wave MIMO prototype: Measurements and experimental results," *IEEE Commun. Mag.*, vol. 56, no. 1, pp. 202–209, Jan 2018.
- [19] W. Roh, J. Y. Seol, J. Park, B. Lee, J. Lee, Y. Kim, J. Cho, K. Cheun, and F. Aryanfar, "Millimeter-wave beamforming as an enabling technology for 5G cellular communications: Theoretical feasibility and prototype results," *IEEE Commun. Mag.*, vol. 52, no. 2, pp. 106–113, Feb. 2014.
- [20] D. Kurita, D. Kitayama, K. Tateishi, A. Harada, Y. Kishiyama, S. Itoh, H. Murai, J. J. Fwu, X. J. Zhuang, K. Stewart, A. Simonsson, and P. Ökvist, "Outdoor experiments on 5G radio access using BS and UE beamforming in 28-GHz frequency band," in *Proc. IEEE CCNC*, Jan. 2019.
- [21] R. J. Weiler, W. Keusgen, A. Maltsev, T. Kühne, A. Pudseyev, Liang Xian, J. Kim, and M. Peter, "Millimeter-wave outdoor access shadowing mitigation using beamforming arrays," in *Proc. IEEE EuCAP*, April 2016.
- [22] A. Thornburg and R. W. Heath, "Ergodic capacity in mmWave ad hoc network with imperfect beam alignment," in *Proc. IEEE MILCOM*, Oct. 2015.
- [23] J. Wildman, P. H. J. Nardelli, M. Latva-aho, and S. Weber, "On the joint impact of beamwidth and orientation error on throughput in directional wireless poisson networks," *IEEE Trans. Wireless Commun.*, vol. 13, no. 12, pp. 7072–7085, Dec. 2014.
- [24] SiversIMA, "Product brief: TRX BF/01," 2018. [Online]. Available: https://www.siversima.com/wp-content/uploads/PB_TRX-BF01_v1-02.pdf

- [25] M. K. Samimi and T. S. Rappaport, “3-D millimeter-wave statistical channel model for 5G wireless system design,” *IEEE Trans. Microw. Theory Tech.*, vol. 64, no. 7, pp. 2207–2225, Jul. 2016.
- [26] Land NRW, “TIM-online 2.0,” NRW, Germany, 2019. [Online]. Available: <https://www.tim-online.nrw.de/tim-online2/>
- [27] ITU-R Resolution 238 (WRC-15), “Studies on frequency-related matters for International Mobile Telecommunications identification including possible additional allocations to the mobile services on a primary basis in portion(s) of the frequency range between 24.25 and 86 GHz for the future development of International Mobile Telecommunications for 2020 and beyond.” 2015.
- [28] SiversIMA, “Product brief: EVK06002,” 2018. [Online]. Available: https://www.siversima.com/wp-content/uploads/PB_EVK-06002-00_1-02-1.pdf
- [29] —, “Product brief: FC1005V/00 V-band converter with LO,” 2017. [Online]. Available: <https://www.siversima.com/wp-content/uploads/FC1005V00-Data-Sheet.pdf>
- [30] Flann Microwave, “Product brief: Standard gain horns series 240,” 2016. [Online]. Available: <https://flann.com/wp-content/uploads/2016/01/Series-240.pdf>
- [31] “Frequenzplan gemäß §54 TKG über die Aufteilung des Frequenzbereichs von 0 kHz bis 3000 GHz auf die Frequenznutzungen sowie über die Festlegungen für diese Frequenznutzungen,” BNetzA, Mar. 2018.
- [32] K. King. (2018, Sep.) Meanwhile, back in the lab, another 5G milestone – Verizon and Samsung reach multi-gigabit throughput over 5G NR and mmwave spectrum. [Online]. Available: <https://www.verizon.com/about/news/meanwhile-back-lab-another-5g-milestone--verizon-and-samsung-reach-multi-gigabit-throughput>
- [33] “LTE; evolved universal terrestrial radio access (E-UTRA); radio frequency (RF) system scenarios,” ETSI 3GPP, TR 36.942 version 14.0.0 Release 14, Apr. 2017.
- [34] “Study on new radio access technology: Radio frequency (RF) and co-existence aspects,” ETSI 3GPP, TS 38.101-2 V14.2.0, Sep. 2017.
- [35] J. Arnold, L. Simić, and P. Mähönen, “Experimental feasibility study of motion sensor-aided mm-wave beam tracking,” in *Proc. ACM mmNets Workshop*, Snowbird, Utah, 2017.
- [36] L. Simić, J. Arnold, M. Petrova, and P. Mähönen, “RadMAC: radar-enabled link obstruction avoidance for agile mm-wave beamsteering,” in *Proc. ACM HotWireless*, 2016.
- [37] M. K. Haider and E. W. Knightly, “Mobility resilience and overhead constrained adaptation in directional 60 GHz WLANs: protocol design and system implementation,” in *Proc. ACM MobiHoc*, Paderborn, Germany, 2016.
- [38] A. Zhou, L. Wu, S. Xu, H. Ma, T. Wei, and X. Zhang, “Following the shadow: Agile 3-D beam-steering for 60 GHz wireless networks,” in *Proc. IEEE INFOCOM*, Apr. 2018.
- [39] A. Alammouri, J. Mo, B. L. Ng, J. C. Zhang, and J. G. Andrews, “Hand grip impact on 5G mmWave mobile devices,” *IEEE Access*, vol. 7, pp. 60 532–60 544, 2019.